Ultrafast Pump–Probe Microscopy on 2D Transition Metal Dichalcogenides

Stephen Boandoh, Fu-He Hsiao, Bongki Shin, Majvor Mack, Linus P. Grote, Rongbin Wang, Yimo Han, Jun Lou, Norbert Koch, Norbert H. Nickel, Chih-Wei Luo, and Yu-Tsung Tsai*

Although microscopic techniques have been used to characterize transition metal dichalcogenides (TMDs), direct observation of charge carrier dynamics distribution in TMDs with diverse shapes remains unexplored. Herein, ultrafast pump–probe microscopy (UPPM) is employed to reveal the carrier dynamics distribution in molybdenum disulfide (MoS_2) and tungsten disulfide (WS_2) monolayer of four shapes: triangular (t-MoS_2), curved triangular (c-MoS_2), triangular (t-WS_2), and hexagonal (h-WS_2). Monitoring the photon transmission T at 1.55 eV after pumping with a photon energy of 3.1 eV, a negative $\Delta T/T$ occurs in t-MoS_2 and c-MoS_2, while a positive $\Delta T/T$ is detected in t-WS_2 and h-WS_2 after 3–7 ps time evolution. This distinctive behavior is attributed to deep/shallow defects below the conduction band minimum (CBM) in MoS_2 and WS_2. Spatial-independent $\Delta T/T$ is observed in t-MoS_2 and t-WS_2, while the $\Delta T/T$ in c-MoS_2 has a rapid decay of photoexcited carriers at the vertices and curved edges. Additionally, a threefold symmetry of $\Delta T/T$ is revealed in h-WS_2, attributed to the dissimilar occupation of defect states near the h-WS_2 CBM. This work paves the way for examining charge carrier dynamics of various shapes of TMDs and provides a unique microscopic method for studying the charge carrier dynamics in emerging TMDs heterostructures.

1. Introduction

Transition metal dichalcogenides (TMDs) have attracted enormous attention recently because of their intriguing physical properties such as strong Coulomb interactions, distinctive spin-valley physics,[1] tunable mechanical,[2] magnetic,[3] optical,[4] and electronic properties,[5] making them ideal materials for application in field-effect transistors (FETs),[6] photodetectors,[7] energy conversion,[8] photonic devices,[9] amongst others. The properties of TMDs, like other 2D materials are related to their structure, size, number of layers, crystal orientations, defects, and morphologies, which can be precisely controlled during growth. Recent studies have demonstrated shape-dependent properties of chemical vapor deposition (CVD) grown TMDs attributed to different levels of defects in the tailored morphologies, making them ideal materials for electrocatalysis and optoelectronics.[10] For example, Zhang et al., reported a threefold increase in photoluminescence (PL) intensity in hexagonal molybdenum disulfide (MoS_2) compared to PL observed in

S. Boandoh, M. Mack, L. P. Grote, N. H. Nickel, Y.-T. Tsai
Helmholtz-Zentrum Berlin für Materialien und Energie GmbH
Institut für Silizium Photovoltaik
12489 Berlin, Germany
E-mail: yu-tsung.tsai@helmholtz-berlin.de

F.-H. Hsiao, C.-W. Luo
Department of Electrophysics
National Yang Ming Chiao Tung University
Hsinchu 30010, Taiwan

B. Shin, Y. Han, J. Lou
Materials Science and NanoEngineering Department
Rice University
Houston, TX 77005-1827, USA

R. Wang, N. Koch
Institut für Physik & IRIS Adlershof
Humboldt-Universität zu Berlin
12489 Berlin, Germany

N. Koch
Helmholtz-Zentrum Berlin für Materialien und Energie GmbH
Forschergruppe Hybride Materialsysteme
12489 Berlin, Germany

C.-W. Luo
Institute of Physics and Center for Emergent Functional Matter Science
National Yang Ming Chiao Tung University
Hsinchu 30010, Taiwan

C.-W. Luo
National Synchrotron Radiation Research Center (NSRRC)
Hsinchu 30076, Taiwan

The ORCID identification number(s) for the author(s) of this article can be found under https://doi.org/10.1002/adpr.202200046.

triangular, tetragonal, and pentagonal shape MoS_2 crystals, due to varying defect distribution in these morphologies.[11] Furthermore, nonuniform alternating domains with bright and dark PL emission apparent in hexagonal tungsten disulfide (h-WS_2) are attributed to the tungsten and sulfur vacancies in this morphology.[12–14] In catalysis, the shape and edge-structure of WS_2 and MoS_2 is considered a dynamic function for hydrogen evolution reaction (HER) due to the existence of varying metal and chalcogen vacancies in these materials.[11,15]

According to the laws of thermodynamics, all crystals grown above 0 K have some level of defects.[16,17] Such defects result in detrimental consequences such as unstable operational circuits, photoluminescence quenching, weak photosensing capabilities, and intense fluctuating of carrier dynamics of 2D materials.[18–22] Although extensive defect studies have been carried out with techniques such as micro-Raman scattering, PL, X-Ray photoelectron spectroscopy, high-angle annular dark-field scanning transmission electron microscopy (HAADF-STEM), and scanning tunneling microscope (STM),[18,23–27] visualization of the dynamics of charge carriers, which is essential in photonic applications, cannot be realized with these techniques. This has necessitated the employment of a nondestructive and time-efficient technique such as time-resolved optical pump–probe spectroscopy for direct probing and visualization of the charge carrier dynamics in TMDs. Information on the excited-state lifetime is beneficial for practical applications. On one hand, optical switches[28] rely on the short photocarrier lifetimes in materials. On the other hand, light-emitting devices[29] favor the long radiative lifetime of photocarriers for enhancement of luminescence quantum yield. The basic principle of time-resolved pump–probe microscopy is based on triggering the optical response of samples under investigation with a high-intensity pump pulse. The dynamics of the process is investigated by using a weak probe beam delayed with respect to the pump beam.[30,31] Despite of strong Coulomb interactions and strong electron-hole concurrence in TMDs, the dynamics of charge carriers can be visualized to estimate the changes in carrier lifetimes and defect distribution in TMDs.[32] While several ultrafast investigations have been carried out with diverse TMDs such as MoS_2,[33] WS_2,[34] $MoSe_2$,[35] WSe_2,[36] and CdSe,[37] little or no work has been done on comparing the charge carrier dynamic distributions in shape-dependent MoS_2 and WS_2 samples.

In this article, we employ time-resolved pump–probe microscopy to reveal the shape-dependent carrier dynamics in MoS_2 and WS_2 morphologies. In these experiments, transient transmittance changes ($\Delta T/T$) are used to observe the ultrafast dynamics in four morphologies of CVD grown TMDs comprising triangular MoS_2 (t-MoS_2), curved triangular MoS_2 (c-MoS_2), triangular WS_2 (t-WS_2), and hexagonal WS_2 (h-WS_2). Ultrafast probing of the carrier dynamics in t-MoS_2 and t-WS_2 revealed position-independent $\Delta T/T$. However, the $\Delta T/T$ in c-MoS_2 is sensitive to position, where a quick decay of photoexcited carriers occurs at the curved edge and vertices. In addition, position-dependent $\Delta T/T$ and threefold symmetry is observed in h-WS_2, with defect states as the proposed mechanism. Additionally, with the same pump–probe transmission, a negative transient transmittance is observed in both t-MoS_2 and c-MoS_2 while a positive transient transmittance occurs in both t-WS_2 and h-WS_2 samples after 3–7 ps (defect-dependent),

which we attribute to the different defect states in the two materials. The results of carrier dynamic distribution in this work will provide knowledge on specific areas of optoelectronic device fabrication when using MoS_2 or WS_2 of desired shapes.

2. Results and Discussion

Figure 1a shows the schematic depiction of the optical ultrafast pump–probe microscopy (UPPM) setup used for the ultrafast dynamic measurements of MoS_2 and WS_2 samples (See experimental section for details). For the spatial-resolved ultrafast carrier dynamics, a scanning microscope combined with the pump–probe system is adopted to map the MoS_2 or WS_2. By controlling the time delay between pump and probe pulses, the position-dependent transient transmittance changes ($\Delta T/T$) can be obtained. The measured $\Delta T/T$ can be expressed as[38]

$$\frac{\Delta T}{T} \approx -2\eta_0 \frac{\Delta\sigma_r}{1+n_s} - 2\eta_0^2 \frac{(\sigma_r\Delta\sigma_r + \sigma_i\Delta\sigma_i)}{(1+n_s)^2} \qquad (1)$$

where $\sigma_r(\sigma_i)$ is the real (imaginary) part of the sample optical conductivity, $n_s \approx 1.45$ is the refractive index of the substrate, and η_0 is the free space impedance. When $\eta_0\sigma_r$ and $\eta_0\sigma_i$ are $\ll$ 1 at the probe energy,[32] the second term on the right-hand side in Equation (1) becomes much smaller than the first term. Therefore, the differential transmission is predominantly affected by changes in the real part of the optical conductivity as expressed in the first term on the right-hand side, as a result of intraconduction band and intravalence band.[32]

To check the sample quality, standard micro-Raman mapping measurements on an as-grown t-MoS_2 were carried out. The data shown in Figure 1b reveals a uniform spatial map of the in-plane E^1_{2g} phonon mode. In addition, the Raman spectrum of E^1_{2g} and A_{1g} modes are extracted from the vertex, edge, and center of t-MoS_2, which confirms the uniformity of the t-MoS_2 sample (see Figure S1a,b, Supporting Information). All samples are characterized in the same fashion prior to pump–probe measurements. Three individual $\Delta T/T$ measurements are then performed at the vertex, edge, and center of t-MoS_2 (inset of Figure 1c). As plotted in Figure 1c, all three single-point $\Delta T/T$ measurements exhibited near-identical absorption strength and decay behavior, indicating a homogeneous carrier dynamic distribution. Transient transmittance microscopy of the same sample further revealed a uniform transmission behavior distribution from 0 to 40 ps (Figure 1d), confirming a similar transmittance relaxation time over the entire area of t-MoS_2 flake. As a result, the uniform photoexcited carrier dynamic distribution of t-MoS_2 is directly observed with our UPPM.

Next, c-MoS_2 is examined in the same fashion. As shown in the micro-Raman mapping image of the in-plane E^1_{2g} mode of c-MoS_2, the intensity of the E^1_{2g} is low at the vertices and at the edges compared to the center where a fairly uniform intensity is obtained (**Figure 2**a). Representative Raman spectrum extracted from spots A–C reveal varying Raman intensities at the vertices, edge, and center (see Figure S2, Supporting Information), which
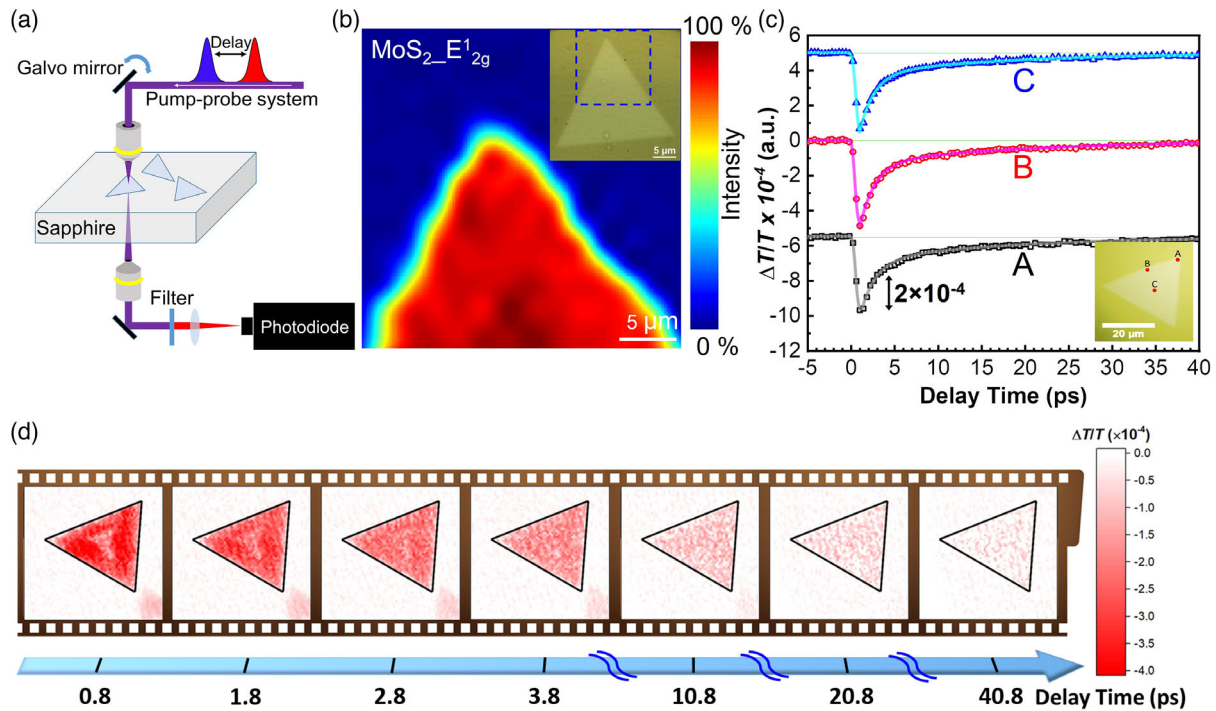
Figure 1. Ultrafast pump–probe microscopy (UPPM) of triangular MoS$_2$. a) Schematic of the time-resolved microscope with pump–probe spectroscopy. b) Micro-Raman mapping of E$^1_{2g}$ mode of t-MoS$_2$ with the scan size indicated in the inset. c) Single-point transient transmittance changes $\Delta T/T$ of t-MoS$_2$ measured at selected spots (A–C) in the inset. d) UPPM images of the transient transmittance change $\Delta T/T$ from 0.8 to 40.8 ps of the same t-MoS$_2$ flake in (c).
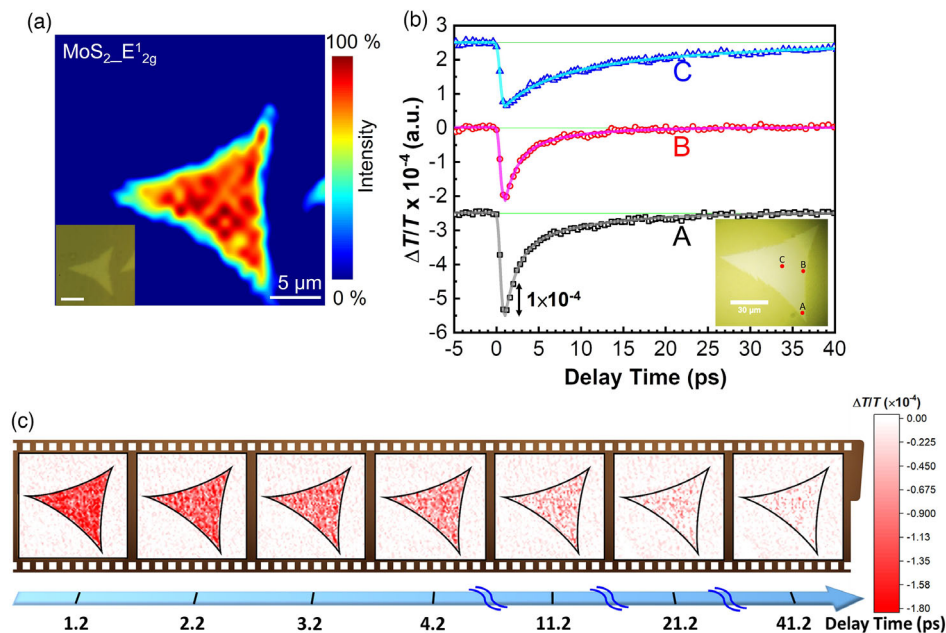
Figure 2. Ultrafast dynamic distribution of curved MoS$_2$. a) Micro-Raman mapping of E$^1_{2g}$ mode of c-MoS$_2$ shown in the bottom left inset. b) Single-point transient transmittance changes $\Delta T/T$ of c-MoS$_2$ measured at selected spots (A–C) in the inset. c) UPPM images of the transient transmittance change $\Delta T/T$ from 1.2 to 41.2 ps of the same c-MoS$_2$ flake in (b).

could be related to defect-induced strain. It should be noted that, though defect-induced strain causes changes in the vibrational modes of MoS$_2$ flakes, no apparent shift in the vibrational modes could be observed in our Raman measurements. This could be due to insufficient strain from low defect concentrations that could not be detected in these Raman measurements.[12,13]

**ADVANCED
SCIENCE NEWS**
www.advancedsciencenews.com

**ADVANCED
PHOTONICS
RESEARCH**
Open Access
www.adpr-journal.com

This Raman response of defect-induced strain suggests that photoexcited carriers can be trapped with these additional defect states. Figure 2b depicts three individual $\Delta T/T$ transients measured at the vertex, edge, and center of c-MoS$_2$ (see inset of Figure 2b). The relaxation time of photoexcited carriers at the vertex and the edge (location A and B) are shorter than the relaxation time in the center (location C), indicating a non-uniform distribution of localized trapping states in c-MoS$_2$. As a result, a nonuniform negative $\Delta T/T$ mapping by UPPM is obtained for c-MoS$_2$ flake and shown in Figure 2c. It is apparent from the transient transmittance images that the relaxation times of photoexcited carriers are shorter at the vertices and the edges than in the center of c-MoS$_2$, visualized by the decreasing density of red points with increasing time. UPPM hence confirms this inhomogeneous carrier dynamic distribution in c-MoS$_2$. To provide a much clearer view of the difference in carrier dynamics distribution in t-MoS$_2$ and c-MoS$_2$, the $\Delta T/T$ spectra at each pixel within t-MoS$_2$ (Figure 1d) and c-MoS$_2$ (Figure 2c) are fitted by a double-exponential decay to obtain the spatial distribution of relaxation time (τ_1 and τ_2) (See Figure S3, Supporting Information). It is apparent that both t-MoS$_2$ and c-MoS$_2$ show uniform distribution in shorter relaxation time (τ_1) of several picoseconds. However, for a longer relation time (τ_2) of several tens of picoseconds, the decay at the center (red-dashed circle in Figure S3d, Supporting Infromation) of c-MoS$_2$ is significantly longer than those at the vertices (pink-dashed circle in Figure S3d, Supporting Information). This nonuniform distribution is clearly absent in t-MoS$_2$ as shown in Figure S3b, Supporting Information.

Furthermore, the dynamics of charge carriers in WS$_2$ morphologies are examined. Similar to t- and c-MoS$_2$ samples, **Figure 3**a reveals a uniform micro-Raman mapping of the in-plane E^1_{2g} mode of t-WS$_2$ flake. Raman spectra with the same

intensity and peak position were also observed in both the E^1_{2g} and A_{1g} modes (see Figure S4, Supporting Information). Time-resolved $\Delta T/T$ was then applied to three locations of the t-WS$_2$ flake, and the measured data are depicted in Figure 3b. Before 4 ps delay time, $\Delta T/T$ exhibits a similar behavior compared to the data shown in Figure 1c from t-MoS$_2$, a quick relaxation of negative $\Delta T/T$ at all locations. Interestingly, after 4 ps, a positive $\Delta T/T$ persists for relaxation time longer than 40 ps.

Contrary to the negative $\Delta T/T$ relaxation distribution observed in both t-MoS$_2$ and c-MoS$_2$ as expected from Equation (1), UPPM reveals a positive $\Delta T/T$ distribution in t-WS$_2$ after 3 ps with a slow relaxation as shown in Figure 3c. We attribute the sign change of $\Delta T/T$ t-WS$_2$ to the partially filled shallow defect states near conduction band minimum (CBM). A more detailed mechanism will be elaborated on later.

Lastly, Figure S5c, Supporting Information, shows a uniform micro-Raman mapped image of the in-plane E^1_{2g} mode of the h-WS$_2$ sample. Raman spectra of the in-plane E^1_{2g} and out-of-plane A_{1g} mode analyzed at different locations exhibit the same Raman peak positions and intensities as shown in Figure S5b, Supporting Information. The discrepancy in the threefold symmetry for h-WS$_2$ in our micro-Raman mapping and previous reports[12–14] could result from the low defect concentrations, leading to insufficient strain and therefore, hardly affects the Raman spectra at different domains, as revealed in new and aging WS$_2$ flakes.[39–42] As shown in **Figure 4**a, UPPM measurements reveal a threefold symmetry of negative (red) $\Delta T/T$ and zero (empty) $\Delta T/T$ in h-WS$_2$ before 5 ps, which correlates to the threefold symmetry visible in the optical image of the measured h-WS$_2$ flake (inset of Figure 4b).

We assigned the red regions as α domains and empty regions as β domains.[12–14] These domains were further revealed in ADF-STEM as shown in Figure 4c–e. Figure 4c displays the
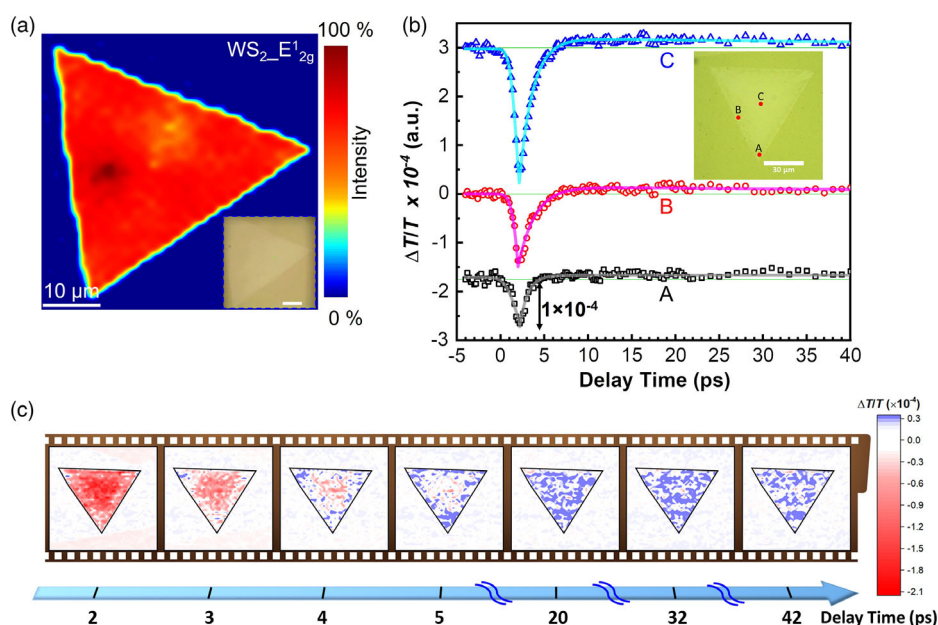
Figure 3. Ultrafast dynamic distribution of triangular WS$_2$. a) Micro-Raman mapping of E^1_{2g} mode of selected t-WS$_2$ depicted in the bottom right inset. b) Single-point transient transmittance changes $\Delta T/T$ of t-WS$_2$ measured at selected spots (A–C) in the inset. c) UPPM images of the transient transmittance change $\Delta T/T$ from 2 to 42 ps of the same t-WS$_2$ flake in (b).
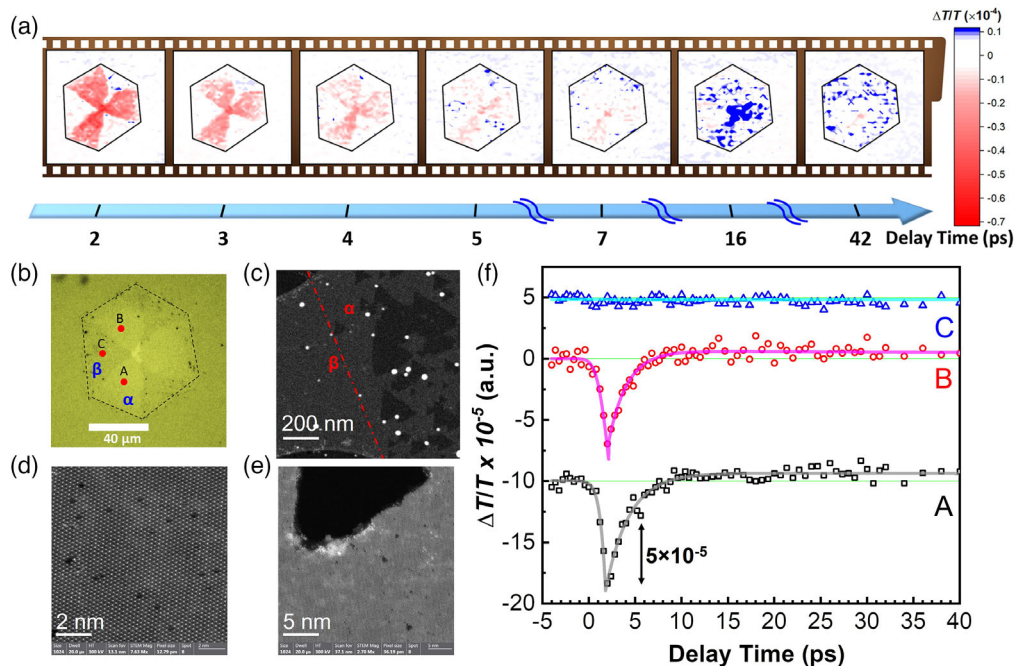
Figure 4. Ultrafast dynamic distribution of hexagonal WS_2. a) UPPM images of the transient transmittance change $\Delta T/T$ from 2 to 42 ps of the same h-WS_2 flake in (b). b) Optical microscopy image reveals alternating α and β domains of h-WS_2. c) Annular dark-field scanning transmission electron microscopy (ADF-STEM) image at the boundary of α and β domain. d) ADF-STEM image at β domain reveals small and sparse defects. e) ADF-STEM image at α domain shows larger defect area. f) Single-point transient transmittance changes $\Delta T/T$ of h-WS_2 measured at selected spots (A–C) in (b).

domain boundary, while Figure 4d,e show the atomic structure and defects in the β domain and α domain, respectively. In the β domain, a few W vacancies are observed (Figure 4d), whereas in the α domain, large triangular defect areas dominate (Figure 4e). Our results are consistent with the previous h-WS_2 study,[14] which also uncovered the defect concentration/sizes with alternating α and β domains by STEM measurements. Upon relaxation after 7 ps, positive $\Delta T/T$ slowly emerges in α domains, similar to the time evolution in Figure 3c. It is worth noting that before 5 ps, the $\Delta T/T$ signal in β domains is too low, exhibiting an empty region in UPPM. Meanwhile, the noises of $\Delta T/T$ in β domains continuously emerge as the blue points in UPPM and require further examination to exclude these contributions. Therefore, three locations in the alternating bright (α) and dark (β) domains of the apparent three-fold symmetry were examined and $\Delta T/T$ plotted in Figure 4f. As shown in the inset of Figure 4b, $\Delta T/T$ at β domain shows no decrease or increase (location C) through pump–probe process. In α domains, in contrast, position-independent $\Delta T/T$ relaxation behavior was revealed (location A and B), similar to the $\Delta T/T$ results in Figure 3b, showing negative $\Delta T/T$ relaxation before 7 ps and a persistent positive $\Delta T/T$ over 40 ps. These results support our direct observation of the carrier dynamic distribution in alternating domains of h-WS_2 by UPPM.

In this section, we present a model to interpret the negative and positive transmittance changes in **Figure 5**. For all samples, the differential transmittance signal would be zero when only probe laser pulse with a photon energy of 1.55 eV is used (below the bandgap of materials), showing a constant transmittance

depicted as $t < 0$ in Figure 5a,b. When the probe laser pulse is applied after a pump laser pulse with a photon energy of 3.1 eV, electrons in the valence band (VB) are excited to the CB, and the transmission of the material changes temporarily, as shown in $t = 0$ in Figure 5a,b. The resulting change in transmission depends on the relaxation behavior of these photoexcited carriers.

In Figure 5a, for t-MoS_2, the pump laser pulse excites electrons from the VB to the middle of the conduction band, filling the energy states near the CBM with relaxation time τ_0. At the same time, electrons from the CBM relax to the deep defect states with relaxation time τ_1 or directly to the VB via phonon assist (or to deeper defect states) with long relaxation time τ_2, during $0 < t < 2$ ps. Because τ_0 is shorter than τ_1, more excited electrons relax back to the CBM before they have a chance to relax into defect states. The accumulated electrons at CBM contribute to negative $\Delta T/T$ even after $t > 5$ ps. Based on this model, more defects exist at the edge and the vertex for c-MoS_2, creating additional relaxation channels for electrons at CBM. As a result, $\tau_{1,edge/vertex}$ should be shorter than $\tau_{1,center}$ (still longer than τ_0), consistent with the slower $\Delta T/T$ recovery at the center (location C) observed in Figure 2b. Consequently, for both t-MoS_2 and c-MoS_2, only negative transmittance recovery to the original transmittance is observed by UPPM shown in red to empty points with time evolution in Figure 2c.

In contrast, for t-WS_2 during $0 < t < 3$–7 ps (defect-dependent), photoexcited electrons relax to CBM with a relaxation time τ_0 while the electrons at CBM relax to the shallow defect states with shorter relaxation time τ_1 ($\tau_1 < \tau_0$) shown in
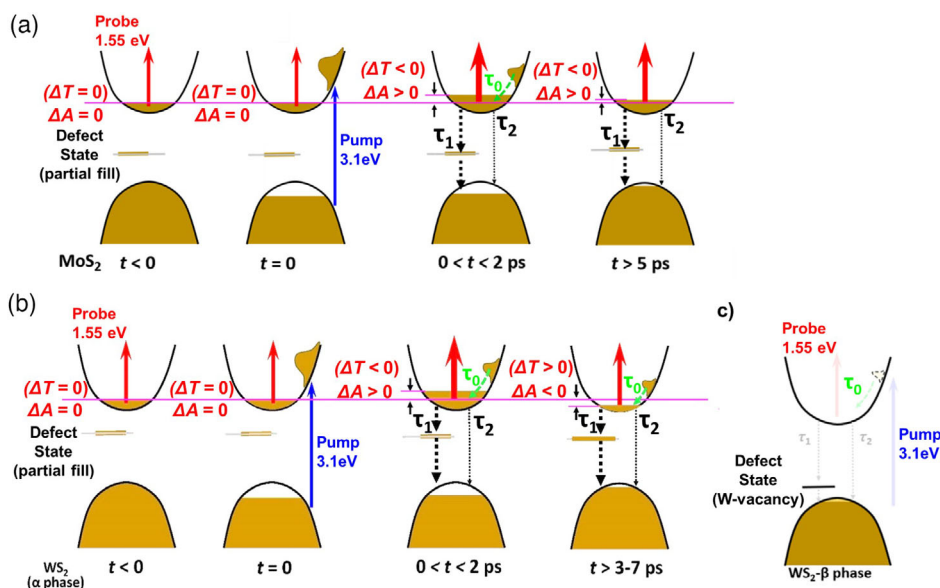
Figure 5. Defects-dependent absorption mechanism. Band diagram sketch and absorption mechanisms of the pump–probe measurements in a) MoS$_2$, b) α phase WS$_2$, c) and β phase WS$_2$. The arrows indicate the pump pulse (blue), the probe pulse (red), and relaxation mechanisms of photoexcited electrons to conduction band minimum (CBM) (green) and electrons at CBM to defect states and valence band (VB) (black). The low pump efficiency of β phase WS$_2$ is depicted in the transparent pump– probe process with no $\Delta T/T$ indication in (c).

Figure 5b. For the case of h-WS$_2$, the τ_0 is 1.5 ≈ 2.3 ps, which is much longer than 0.4 ps in MoS$_2$. Due to this slow intra-band relaxation of the photoexcited electrons in CB and fast relaxation of the electrons from the CBM into shallow defect states, the unbalance (output rate > input rate) and missing CBM electrons contribute to a positive $\Delta T/T$ observed after 3–7 ps (defect-dependent) in Figure 3b. It is important to note that because of more defects at the edges of t-WS$_2$, CBM electrons at these locations relax to defects earlier than CBM electrons at the center, shown in red to blue points with time evolution by UPPM in Figure 3c. To provide a much clearer view of lifetimes between t-MoS$_2$ and t-WS$_2$ samples, the lifetime fitting and fitting parameters for all samples are provided (See Figure S6, Supporting Information).

Applying the same absorption mechanism from t-WS$_2$ for h-WS$_2$, we describe the threefold symmetry revealed from UPPM as a result of pumping efficiency difference. In α (bright) domains, photo-excited electrons relax to shallow defects or the VB similarly as the photoexcited electrons relax in t-WS$_2$ as shown in Figure 5b; whereas in β (dark) domains, the pumping efficiency is too low because of the low absorption of visible light range in WS$_2$ with W-vacancy[14] and the limited amount of photo-excited electrons result in non-observable transmittance change as indicated in Figure 5c. Thus, we have developed a useful optical tool UPPM, and corresponding transient absorption mechanism to study and visualize carrier dynamic distribution for 2D TMDs morphology. For the future, carrier dynamic distribution of various shapes, grain boundaries, or lateral heterostructure studies on TMDs can be of great interest by applying UPPM.

3. Conclusion

In this work, we investigated the shape-dependent ultrafast dynamics of tailored CVD MoS$_2$ and WS$_2$ morphologies and

showed that carriers in t-MoS$_2$ and t-WS$_2$ flakes behave homogenously in these two samples. A position-dependent relaxation behavior of photoexcited carriers is revealed in c-MoS$_2$ and h-WS$_2$, which we attribute to varying defect states in these morphologies. Additionally, with the same transmission probe photon energy, a negative/positive transmission change observed in MoS$_2$/WS$_2$ sample is discussed with the existence of shallow defect states below CBM of WS$_2$. The faster relaxation of CBM electrons to shallow defect states than the relaxation of photoexcited electrons to CBM leads to the positive transmission change in WS$_2$ samples. Furthermore, a threefold symmetry of photoexcited carriers is observed in h-WS$_2$ flake, which we attributed to S-/W-vacancy defect states near the CBM, resulting in dissimilar pumping efficiency in the alternating domains. Our results provide a paradigm shift in device fabrication, such that, with the revealed carrier behaviors in MoS$_2$ and WS$_2$ samples, one can precisely choose TMDs of desired shapes and carrier dynamics for suitable optoelectronics.

4. Experimental Section

Controlled Growth of Triangular and Curved Triangular MoS$_2$ Flakes: Triangular and curved triangular MoS$_2$ monolayers were synthesized via chemical vapor deposition (CVD) under atmospheric conditions, using a two-zone furnace fitted with a quartz tube of 7 cm in diameter. Prior to growth, a pre-annealed double-side polished 10 × 10 mm^2 sapphire was cleaned and used as the growth substrate. 0.002 M NaMoO$_4$.2H$_2$O as Mo source was coated on the pre-cleaned sapphire. The substrate was then placed at the center of the quartz tube and sufficient sulfur powder was placed upstream, 34 cm from the growth substrate. The quartz tube was then evacuated to 10^{-6} torr and subsequently purged with N$_2$ gas until an atmospheric condition is attained. Next, the oven was heated up to 850 °C in 10 min, and maintained at this temperature for 15 min. For the growth of MoS$_2$ flakes, Ar with a purity of 99.99% was used as the

carrier gas with 60 standard cubic centimeters per minute (sccm) under an inert atmosphere. To obtain triangular MoS_2, the growth substrate was placed face-up in a narrow crucible placed inside the 7 cm diameter quartz tube, to serve as a narrow reaction chamber. Curved triangular MoS_2 was grown by placing the coated sapphire substrate face-up on the back of a quartz boat in the 7 cm diameter quartz tube to serve as a wide reaction chamber.

Controlled Growth of Triangular and Hexagonal WS$_2$ Flakes: Triangular and hexagonal WS_2 monolayers were synthesized via CVD under atmospheric condition, using a two-zone furnace fitted with a quartz tube of 5 cm in diameter. Prior to growth, a pre-annealed double-side polished 10×10 mm sapphire was cleaned and used as the growth substrate. 0.008 M $NaWO_4.2H_2O$ solution was mixed with 60% w/v solution of iodixanol in water (OptiPrep, density gradient medium (Sigma-Aldrich, D1556)) to serve as the W source and coated on the pre-cleaned sapphire. The coated substrate was then placed at the center of the quartz tube and sufficient sulfur powder was placed upstream, 16 cm from the growth substrate. The quartz tube was then evacuated to 10^{-6} torr and subsequently purged with ultra-pure Argon gas till atmospheric pressure is attained. Next, the oven was heated up to 830 °C in 10 min, and maintained at this temperature for 15 min. For the growth of WS_2 flakes, Ar with a purity of 99.99% was used as the carrier gas with 60 sccm under an inert atmosphere. To obtain triangular WS_2, the growth substrate was placed face-up in a narrow crucible placed inside the 5 cm diameter quartz tube, to serve as a narrow reaction chamber. Hexagonal WS_2 was grown by placing the coated sapphire substrate face-up on the back of a quartz boat in the 5 cm diameter quartz tube to serve as a wide reaction chamber.

Micro-Raman Scattering: Raman scattering was performed with a 442 nm Ar-Ion laser focused on the sample using a 100x long-range objective, resulting in a laser spot size of 1 μm^2 at the sample surface. The Raman spectra were obtained with a nitrogen-cooled charge-coupled device (CCD) camera and the spectrum resolution is 0.4 cm^{-1}.

Optical UPPM: The light source is a Ti:sapphire laser (Femtosource scientific XL300, Femtolaser) with a central wavelength of 800 nm, a repetition rate of 5.2 MHz, and a pulse width of 100 fs. For the pump pulses, a β-BaB_2O_4 nonlinear crystal is used to convert the wavelength from 800 nm to 400 nm after an acousto-optic modulator, which modulates the pump beam for the reference frequency of a lock-in amplifier. The polarization of the pump and probe pulses were set to be perpendicular to eliminate the coherent spike around the zero-time delay.[43] Finally, the pump and probe pulses are combined by a dichroic beam splitter and collimated to a microscope system. For the spatial-resolved ultrafast carrier dynamics, a scanning microscope combined with the pump–probe system is adopted to map the MoS_2 or WS_2. Both pump and probe pulses are focused on the sample by an objective after a galvo mirror, which serves the function of spatial mapping. The spatial resolution is about 1.5 μm, and the typical pump and probe fluences amount to 266 and 165 $\mu J\ cm^{-2}$, respectively. By controlling the time delay between pump and probe pulses, the position-dependent transient transmittance changes ($\Delta T/T$) can be obtained.

ADF-STEM Sample Preparation and Characterization: The WS_2 was grown by CVD on a sapphire substrate. The substrate was spin-coated by PMMA with 3000 rpm for 1 minute. The edges of the substrate were scratched using a razor blade to expose the sapphire surface, allowing faster etching. Then, the substrate was floated up onto sodium hydroxide solution with the volume ratio 1:10, NaOH and H_2O respectively. The sapphire substrate was immersed into the solution after being etched off by the solution and the PMMA film with WS_2 flakes stayed onto the solution. The film was transferred to de-ionized (DI) water 3–4 times to clean the residual solution, followed by being fished out by a TEM grid and air-dried. The TEM grid was annealed in a CVD tube furnace under a mixture of 90% N_2% and 10% H_2 at 200 sccm to remove the PMMA. The temperature was increased up to 40° °C with the rate of 1° °C min^{-1}, held at 40° °C for 2 h, and cooled down to room temperature. All ADF-STEM images were taken in a Thermo Fisher Titan Themis operated at 300 kV.

Supporting Information

Supporting Information is available from the Wiley Online Library or from the author.

Conflict of Interest

The authors declare no conflict of interest.

Data Availability Statement

The data that support the findings of this study are available in the supplementary material of this article.

[1] X. Xu, W. Yao, D. Xiao, T. F. Heinz, *Nat. Phys.* **2014**, *10*, 343.

[2] S. Bertolazzi, J. Brivio, A. Kis, *ACS Nano* **2011**, *5*, 9703.

[3] Y. Ma, Y. Dai, M. Guo, C. Niu, Y. Zhu, B. Huang, *ACS Nano* **2012**, *6*, 1695.

[4] Y. J. Zhang, T. Oka, R. Suzuki, J. T. Ye, Y. Iwasa, *Science* **2014**, *344*, 725.

[5] D. Lembke, S. Bertolazzi, A. Kis, *Acc. Chem. Res* **2015**, *48*, 100.

[6] M. Cetina, M. Jag, R. S. Lous, I. Fritsche, J. T. M. Walraven, R. Grimm, J. Levinsen, M. M. Parish, R. Schmidt, M. Knap, E. Demler, *Science* **2016**, *354*, 96.

[7] O. Lopez-Sanchez, D. Lembke, M. Kayci, A. Radenovic, A. Kis, *Nat. Nanotechnol.* **2013**, *8*, 497.

[8] S. Memaran, N. R. Pradhan, Z. Lu, D. Rhodes, J. Ludwig, Q. Zhou, O. Ogunsolu, P. M. Ajayan, D. Smirnov, A. I. Fernández-Domínguez, F. J. García-Vidal, L. Balicas, *Nano Lett.* **2015**, *15*, 7532.

[9] X. Liu, T. Galfsky, Z. Sun, F. Xia, E. C. Lin, Y. H. Lee, S. Kéna-Cohen, V. M. Menon, *Nat. Photonics* **2014**, *9*, 30.

[10] A. M. Van Der Zande, P. Y. Huang, D. A. Chenet, T. C. Berkelbach, Y. You, G. H. Lee, T. F. Heinz, D. R. Reichman, D. A. Muller, J. C. Hone, *Nat. Mater.* **2013**, *12*, 554.

[11] G. Zhang, J. Wang, Z. Wu, R. Shi, W. Ouyang, A. Amini, B. N. Chandrashekar, N. Wang, C. Cheng, *ACS Appl. Mater. Interfaces* **2017**, *9*, 763.

[12] H. Y. Jeong, Y. Jin, S. J. Yun, J. Zhao, J. Baik, D. H. Keum, H. S. Lee, Y. H. Lee, *Adv. Mater.* **2017**, *29*, 1605043.

[13] Y. Sheng, X. Wang, K. Fujisawa, S. Ying, A. L. Elias, Z. Lin, W. Xu, Y. Zhou, A. M. Korsunsky, H. Bhaskaran, M. Terrones, J. H. Warner, *ACS Appl. Mater. Interfaces* **2017**, *9*, 15005.

[14] Y. C. Lin, S. Li, H. P. Komsa, L. J. Chang, A. V. Krasheninnikov, G. Eda, K. Suenaga, *Adv. Funct. Mater.* **2018**, *28*, 1.

[15] T. F. Jaramillo, K. P. Jørgensen, J. Bonde, J. H. Nielsen, S. Horch, I. Chorkendorff, *Science* **2007**, *317*, 100.

[16] H. Schmalzried, F. A. Kröger, *Ber. Bunsen Ges. Phys. Chem.* **1964**, *68*, 608.

[17] F. Kroger, F. Stieltjes, H. Vink, *Philips Res. Rep.* **1959**, *14*, 557.

[18] Y. C. Lin, T. Björkman, H. P. Komsa, P. Y. Teng, C. H. Yeh, F. S. Huang, K. H. Lin, J. Jadczak, Y. S. Huang, P. W. Chiu, A. V. Krasheninnikov, K. Suenaga, *Nat. Commun.* **2015**, *6*, 1.

[19] W. Zhou, X. Zou, S. Najmaei, Z. Liu, Y. Shi, J. Kong, J. Lou, P. M. Ajayan, B. I. Yakobson, J. C. Idrobo, *Nano Lett.* **2013**, *13*, 2615.

[20] Y. Han, T. Hu, R. Li, J. Zhou, J. Dong, *Phys. Chem. Chem. Phys.* **2015**, *17*, 3813.

[21] T. Mueller, E. Malic, *npj 2D Mater. Appl.* **2018**, *2*, 1.

[22] Y. Guo, X. Wei, J. Shu, B. Liu, J. Yin, C. Guan, Y. Han, S. Gao, Q. Chen, *Appl. Phys. Lett.* **2015**, *106*, 103109.

[23] R. Addou, S. McDonnell, D. Barrera, Z. Guo, A. Azcatl, J. Wang, H. Zhu, C. L. Hinkle, M. Quevedo-Lopez, H. N. Alshareef, L. Colombo, J. W. P. Hsu, R. M. Wallace, *ACS Nano* **2015**, *9*, 9124.

[24] J. Lin, S. T. Pantelides, W. Zhou, *ACS Nano* **2015**, *9*, 5189.

[25] J. D. Fuhr, A. Saúl, J. O. Sofo, *Phys. Rev. Lett.* **2004**, *92*, 026802.

[26] X. Zhang, Q. H. Tan, J. Bin Wu, W. Shi, P. H. Tan, *Nanoscale* **2016**, *8*, 6435.

[27] Y. Liu, H. Nan, X. Wu, W. Pan, W. Wang, J. Bai, W. Zhao, L. Sun, X. Wang, Z. Ni, *ACS Nano* **2013**, *7*, 4202.

[28] Z. Sun, A. Martinez, F. Wang, *Nat. Photonics* **2016**, *10*, 227.

[29] M. Amani, D. H. Lien, D. Kiriya, J. Xiao, A. Azcatl, J. Noh, S. R. Madhvapathy, R. Addou, K. C. Santosh, M. Dubey, K. Cho, R. M. Wallace, S. C. Lee, J. H. He, J. W. Ager, X. Zhang, E. Yablonovitch, A. Javey, *Science* **2015**, *350*, 1065.

[30] J. W. You, S. R. Bongu, Q. Bao, N. C. Panoiu, *Nanophotonics* **2018**, *8*, 63.

[31] C. W. Luo, Y. T. Wang, A. Yabushita, T. Kobayashi, *Optica* **2016**, *3*, 82.

[32] H. Wang, C. Zhang, F. Rana, *Nano Lett.* **2015**, *15*, 339.

[33] K. Wang, J. Wang, J. Fan, M. Lotya, A. O'Neill, D. Fox, Y. Feng, X. Zhang, B. Jiang, Q. Zhao, H. Zhang, J. N. Coleman, L. Zhang, W. J. Blau, *ACS Nano* **2013**, *7*, 9260.

[34] Z. E. Eroglu, O. Comegys, L. S. Quintanar, N. Azam, S. Elafandi, M. Mahjouri-Samani, A. Boulesbaa, *Phys. Chem. Chem. Phys.* **2020**, *22*, 17385.

[35] M. F. Lin, V. Kochat, A. Krishnamoorthy, L. Bassman, C. Weninger, Q. Zheng, X. Zhang, A. Apte, C. S. Tiwary, X. Shen, R. Li, R. Kalia, P. Ajayan, A. Nakano, P. Vashishta, F. Shimojo, X. Wang, D. M. Fritz, U. Bergmann, *Nat. Commun.* **2017**, *8*, 1.

[36] Q. Cui, F. Ceballos, N. Kumar, H. Zhao, *ACS Nano* **2014**, *8*, 2970.

[37] M. B. Mohamed, C. Burda, M. A. El-Sayed, *Nano Lett.* **2001**, *1*, 589.

[38] J. M. Dawlaty, S. Shivaraman, J. Strait, P. George, M. Chandrashekhar, F. Rana, M. G. Spencer, D. Veksler, Y. Chen, *Appl. Phys. Lett.* **2008**, *93*, 8.

[39] H. Bretscher, Z. Li, J. Xiao, D. Y. Qiu, S. Refaely-Abramson, J. A. Alexander-Webber, A. Tanoh, Y. Fan, G. Delport, C. A. Williams, S. D. Stranks, S. Hofmann, J. B. Neaton, S. G. Louie, A. Rao, *ACS Nano* **2021**, *15*, 8780.

[40] Z. Wu, Z. Ni, *Nanophotonics* **2017**, *6*, 1219.

[41] S. Salehi, A. Saffarzadeh, *Surf. Sci.* **2016**, *651*, 215.

[42] Y. Yu, X. Zhang, Z. Zhou, Z. Zhang, Y. Bao, H. Xu, L. Lin, Y. Zhang, X. Wang, *Photonics Res.* **2019**, *7*, 711.

[43] C. W. Luo, Y. T. Wang, F. W. Chen, H. C. Shih, T. Kobayashi, *Opt. Express* **2009**, *17*, 11321.

2200046 (8 of 8)